Solution-Processed All-Perovskite Multi-Junction Solar Cells

David P. McMeekin,[1] Suhas Mahesh,[1] Nakita K. Noel,[1] Matthew T. Klug,[1] JongChul Lim,[1] Jonathan H. Warby,[1] James M. Ball,[1] Laura M. Herz,[1] Michael B. Johnston,[1] and Henry J. Snaith[1,2]*

[1]Clarendon Laboratory, Department of Physics, University of Oxford, Parks Road, Oxford, OX1 3PU, UK

[2]Lead Contact

*Correspondence: henry.snaith@physics.ox.ac.uk

SUPPLEMENTARY INFORMATION

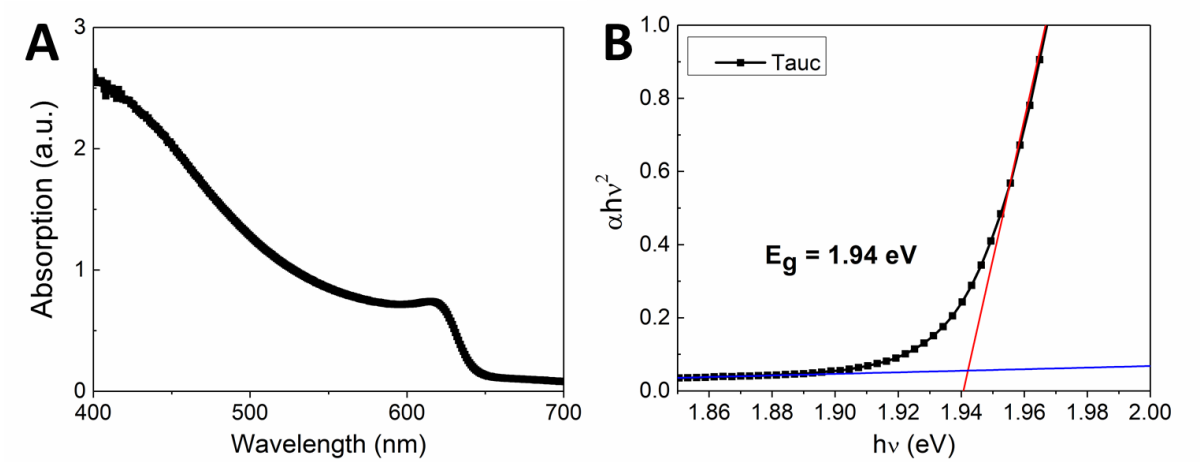

Figure S1 Optical characterization of $FA_{0.83}Cs_{0.17}Pb(Br_{0.7}I_{0.3})_3$ perovskite material with 2% potassium additive A) Absorption spectrum of $FA_{0.83}Cs_{0.17}Pb(Br_{0.7}I_{0.3})_3$ measured with an integration sphere. B) Tauc plot of **$FA_{0.83}Cs_{0.17}Pb(Br_{0.7}I_{0.3})_3$** perovskite assuming direct band gap material and fitting of optical band gap from intercept.

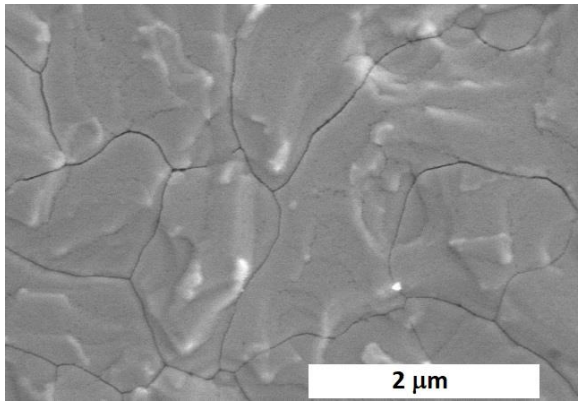

Figure S2 Scanning electron microscopy (SEM) image of the top view of $FA_{0.83}Cs_{0.17}Pb(Br_{0.7}I_{0.3})_3$ perovskite film.

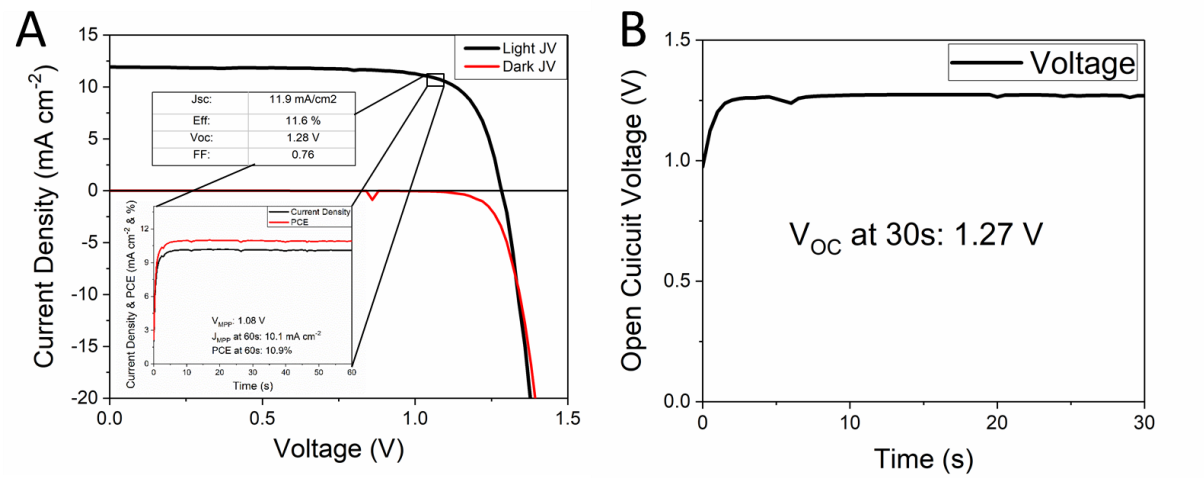

Figure S3 Current-voltage characteristic of a SnO_2/PCBM/$FA_{0.83}Cs_{0.17}Pb(Br_{0.7}I_{0.3})_3$/Spiro-OMeTAD perovskite solar cell with 2% mol. potassium (K^+) additive. A) Forward bias to short-circuit current-voltage curve measured under simulated air-mass (AM) 1.5, using a 0.25V/s scan rate. The inset figure shows the photocurrent density and power conversion efficiency measured at the maximum power point for a 60s time span. **B)** Stabilized open circuit voltage (V_{oc}) of $FA_{0.83}Cs_{0.17}Pb(Br_{0.7}I_{0.3})_3$ heterojunction perovskite solar cell.

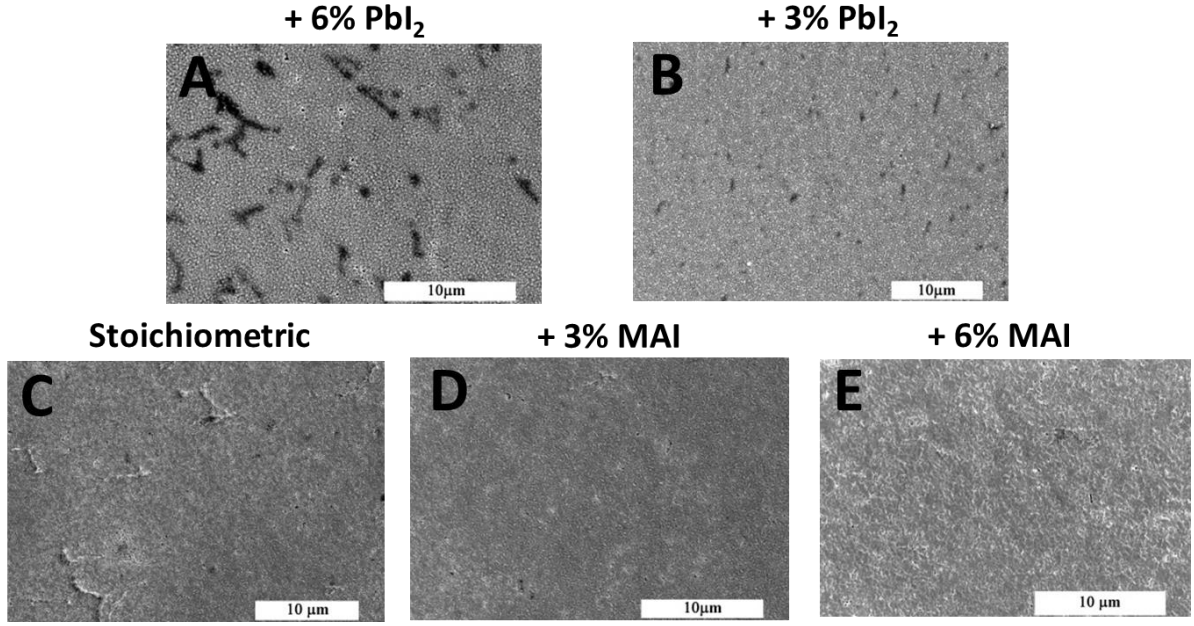

Figure S4 Scanning electron microscopy (SEM) image of the top view of $MAPbI_3$ thin film deposited on top of the front-cell and interlayer, prepared using an acetonitrile(CH_3CN)/methylamine(CH_3NH_2) (ACN/MA) solvent system, ranging from excess 6% PbI_2 to excess 6% MAI.

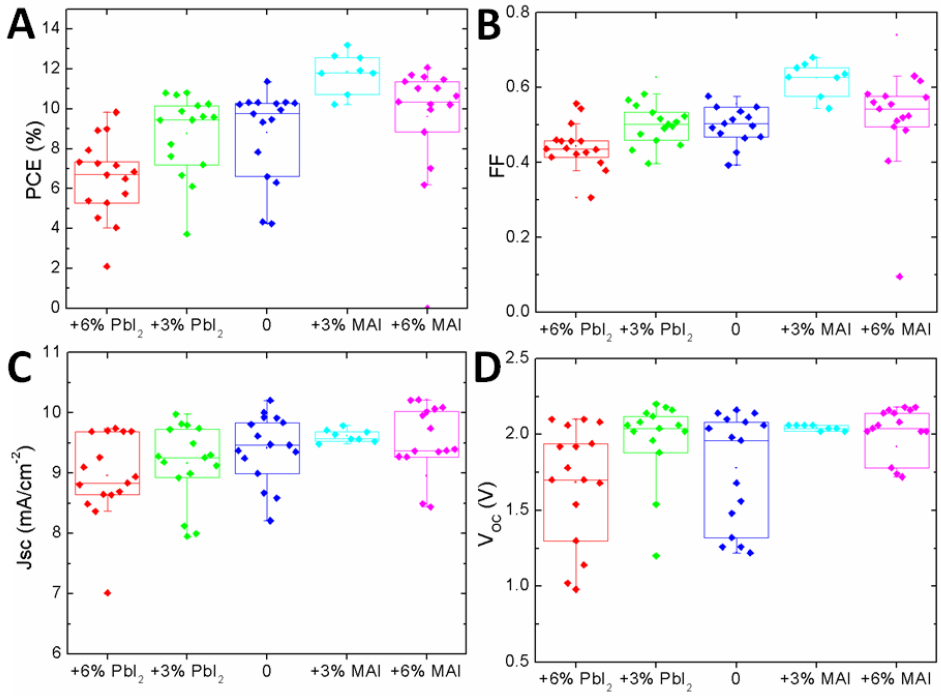

Figure S5 Impact of varying the composition of A to B-site cations of the ACN/MA $MAPbI_3$ perovskite system in the SnO_2/PCBM/$FA_{0.83}Cs_{0.17}Pb(Br_{0.7}I_{0.3})_3$/Spiro-OMeTAD/PEDOT:PSS/ITO NPs/PCBM/$MAPbI_3$/Spiro-OMeTAD tandem architecture structure. A) Power conversion efficiency B) Fill-factor C) Short-circuit current density D) Open-circuit voltage.

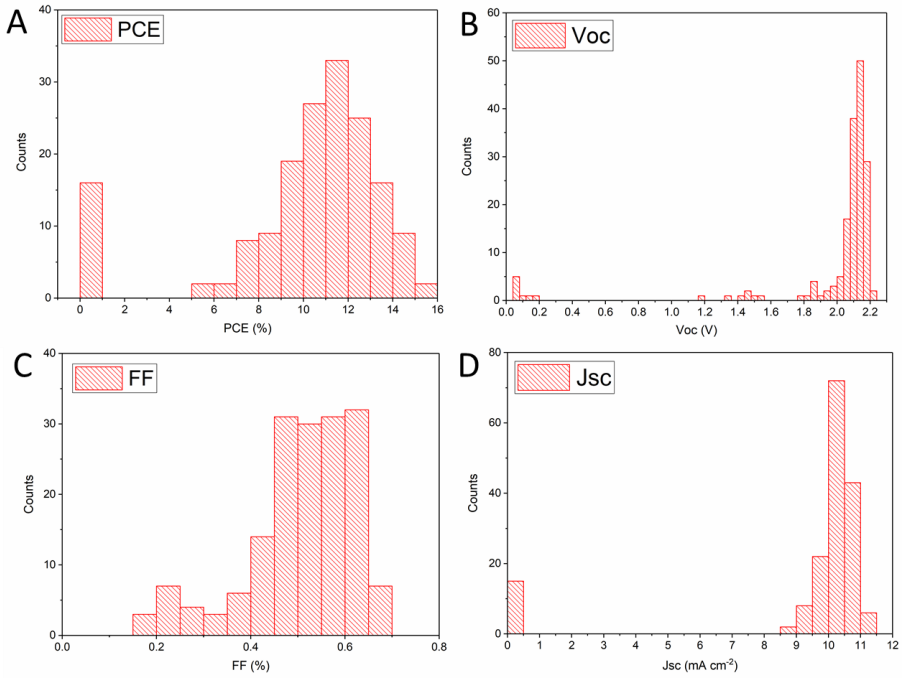

Figure S6 Histogram of the performance of the $FA_{0.83}Cs_{0.17}Pb(Br_{0.7}I_{0.3})_3$/$MAPbI_3$ tandem solar cell perovskite. A) JV Power conversion efficiency (PCE). B) Open-circuit voltage (V_{oc}). D) Fill-factor (FF). C) Short-circuit current-density (J_{sc}).

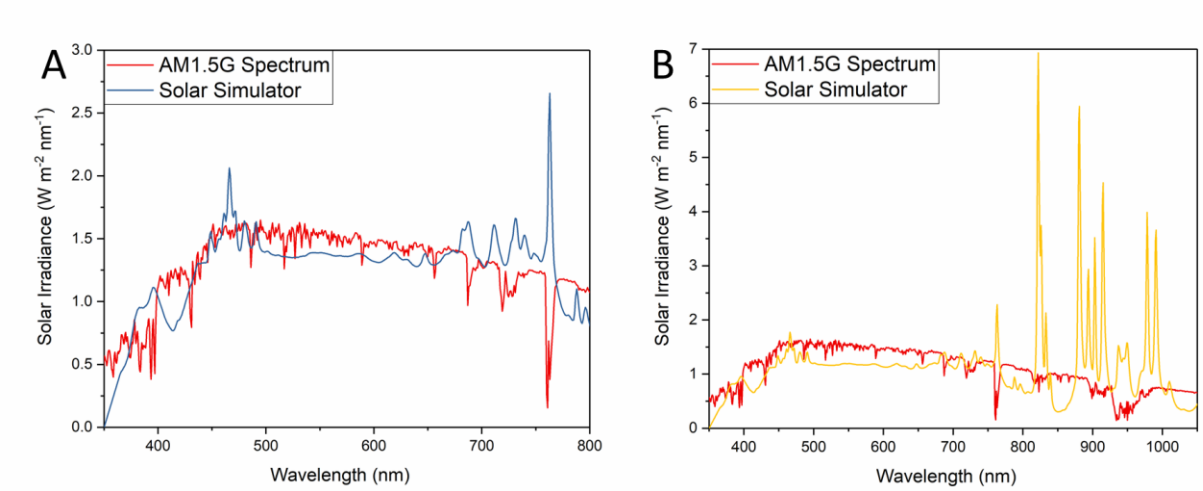

Figure S7 Measured solar simulator spectrum compared to the AM1.5G spectrum. A) Xenon lamp spectrum used for the measurement of the $FA_{0.83}Cs_{0.17}Pb(Br_{0.7}I_{0.3})_3$/$MAPbI_3$ tandem solar cell B) Xenon lamp spectrum used for the measurement of the $FA_{0.83}Cs_{0.17}Pb(Br_{0.7}I_{0.3})_3$/$MAPbI_3$/$MAPb_{0.75}Sn_{0.25}I_3$ triple-junction solar cell.

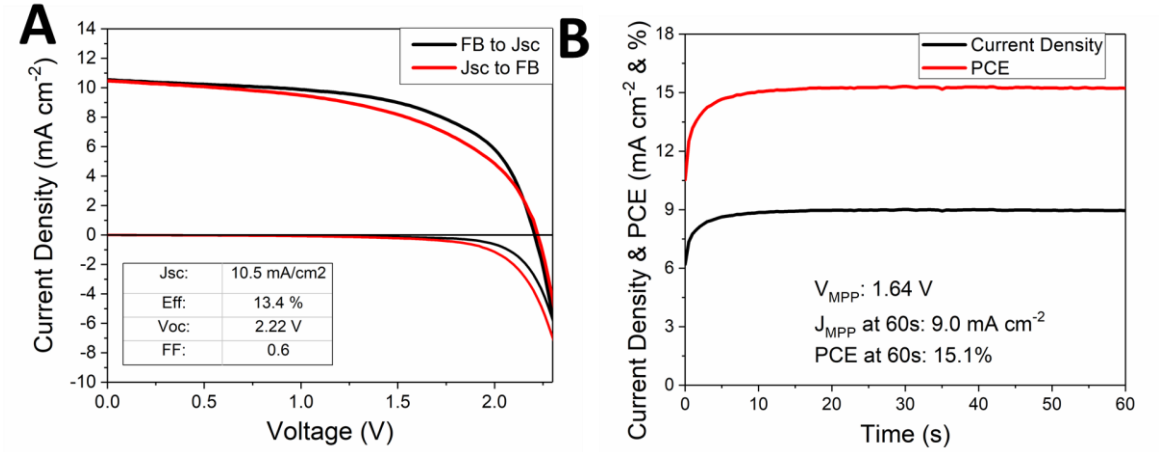

Figure S8 Device performance of a $FA_{0.83}Cs_{0.17}Pb(Br_{0.7}I_{0.3})_3$/$MAPbI_3$ tandem solar cell with the highest open circuit voltage A) Current-voltage characteristics, measured under simulated air-mass (AM) 1.5 sunlight, using a 0.25V/s scan rate. B) Photocurrent density and power conversion efficiency measured at the maximum power point for a 60 s time span. A mismatch factor of 1.004 has been applied to the PCE.

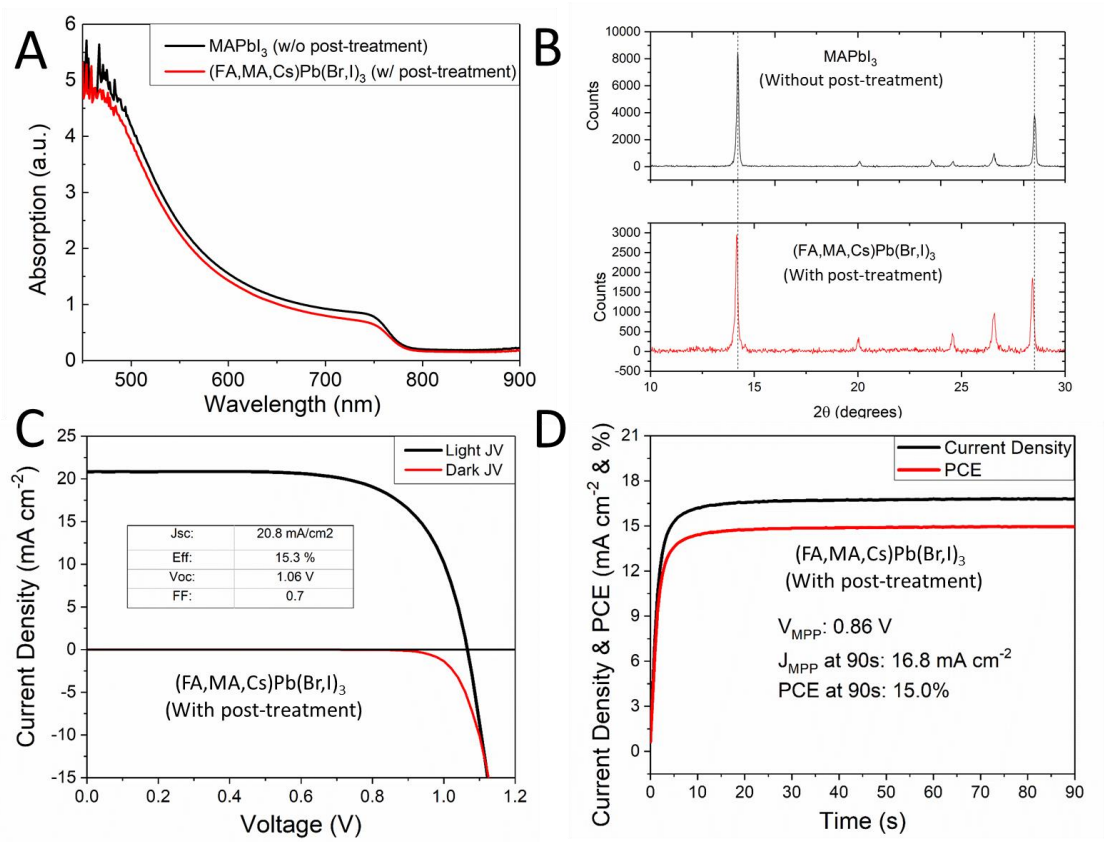

Figure S9 Impact of the FAI/CsBr in MeOH post-treatment on the absorption onset, crystal structure and device performance of the $MAPbI_3$ processed via the ACN/MA solvent system. A) Absorption spectrum and B) XRD-diffraction pattern shown before and after deposition of the FAI/CsBr in MeOH post-treatment. C) Current-voltage characteristics, measured under simulated air-mass (AM) 1.5 sunlight using a 0.25V/s scan rate. D) Photocurrent density and power conversion efficiency measured at the maximum power point for a 90 s time span. A mismatch factor of 1.004 has been applied to the PCE.

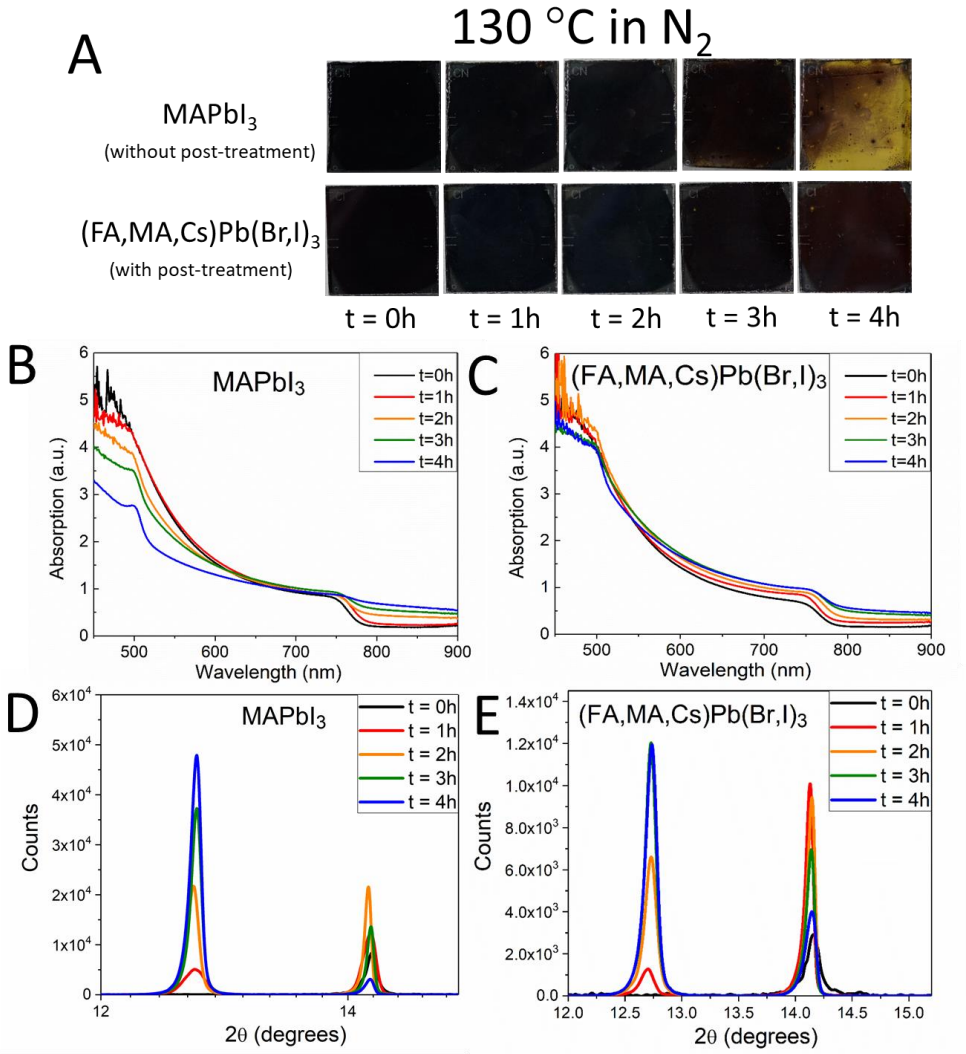

Figure S10 Impact of the FAI/CsBr in MeOH post-treatment on the thermal stability of the $MAPbI_3$ processed via the ACN/MA solvent system. A) Photographs of a $MAPbI_3$ fabricated via the ACN/MA solvent system thin film with and without the post-treatment. The perovskite films were stressed at 130° C in a nitrogen atmosphere. B,C) Ultraviolet-visible absorbance spectra of corresponding films. D,E) XRD-diffraction pattern of corresponding films.

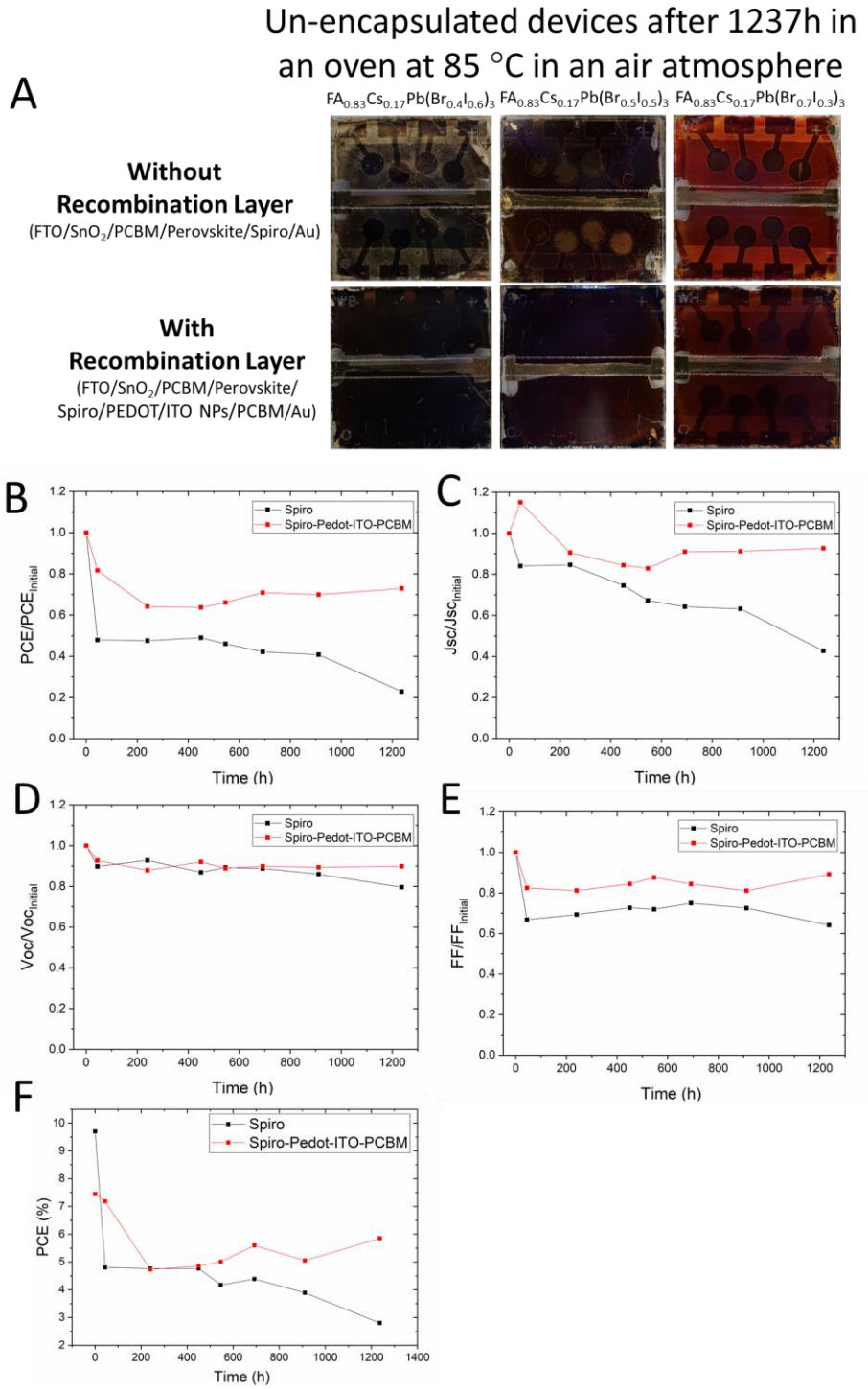

Figure S11 Impact of the added recombination layer along with the PCBM electron accepting layer on the thermal stability of the perovskite device. **The 40 devices were stressed at 85° C in an oven in an air atmosphere.** A) Photographs of $FA_{0.83}Cs_{0.17}Pb(I_{(1-y)}Br_y)_3$ devices with and without the added Pedot/ITO NPs recombination layer and the PCBM electron accepting layer. Impact of temperature on the average B) $PCE/PCE_{Initial}$, C) $Jsc/Jsc_{Initial}$, D) $Voc/Voc_{Initial}$, E) $FF/FF_{Initial}$ F) PCE.

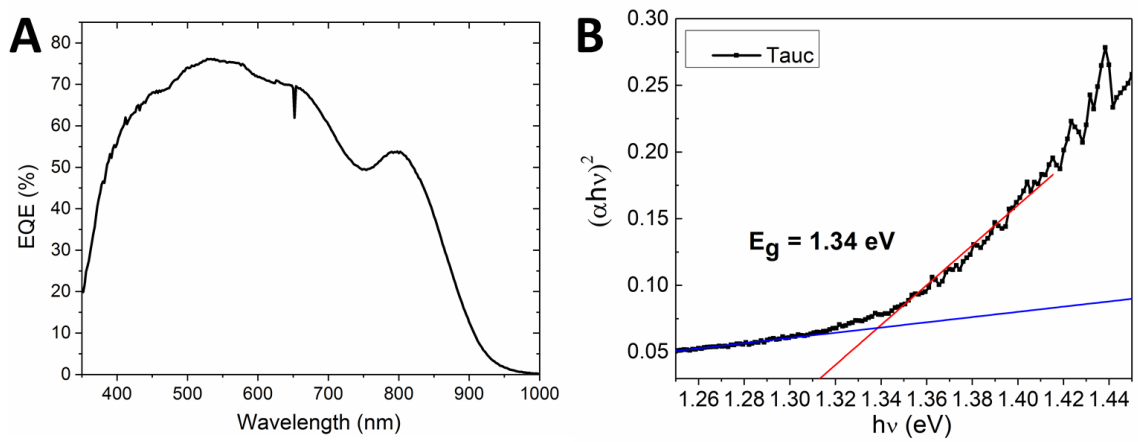

Figure S12 Characterization of $MAPb_{0.75}Sn_{0.25}I_3$ perovskite material A) External quantum efficiency (EQE) spectrum for a FTO/SnO_2/$PC_{61}BM$/$MAPb_{0.75}Sn_{0.75}I_3$/Spiro(TFSI)$_2$ solar cells architecture, measured using a 50 Ω resistive load. B) Tauc plot of $MAPb_{0.75}Sn_{0.25}I_3$ perovskite material assuming direct band gap material.

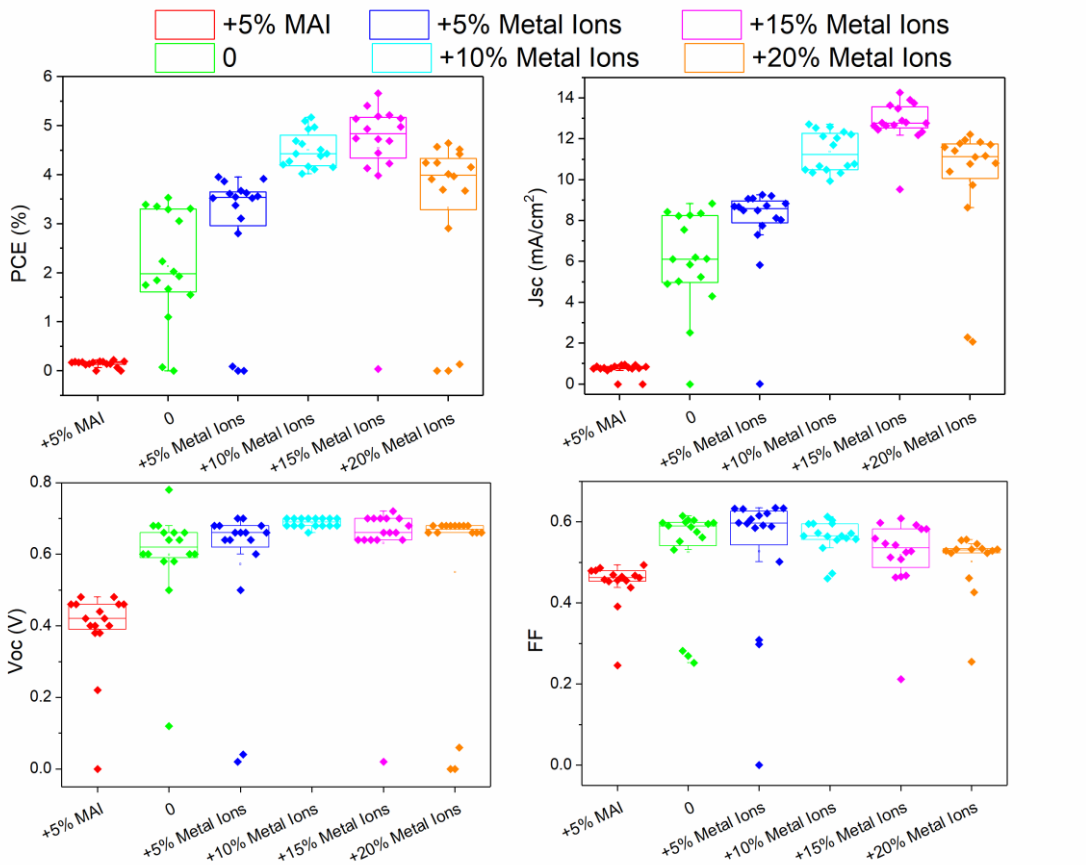

Figure S13 Impact of varying the composition of A to B-site cations of the ACN/MA $MAPb_{0.75}Sn_{0.25}I_3$ single junction perovskite system on A) power conversion efficiency B) fill-factor C) short-circuit current density D) open-circuit voltage.

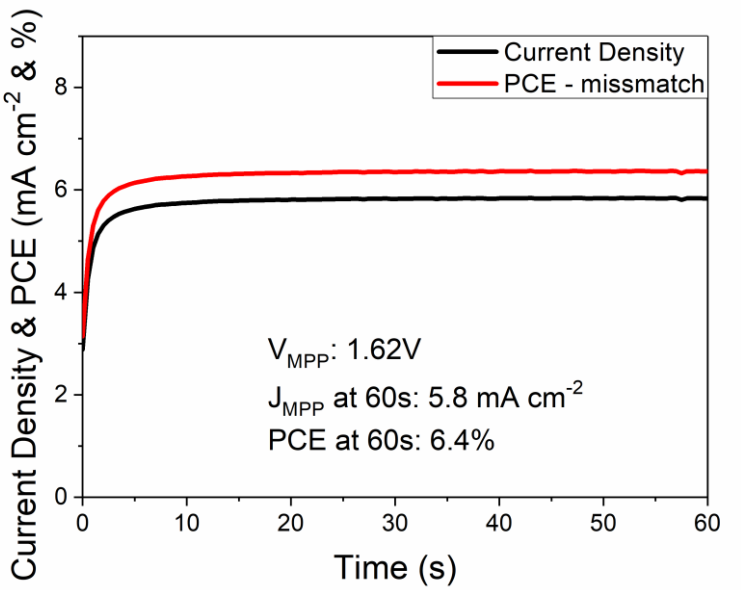

Figure S14 Device performance of a $FA_{0.83}Cs_{0.17}Pb(Br_{0.7}I_{0.3})_3$/$MAPbI_3$/$MAPb_{0.75}Sn_{0.25}I_3$ triple-junction solar cells with the highest open circuit voltage A) Current-voltage characteristic measured under simulated sunlight, , with an equivalent irradiance of 98.8 mW cm^{-2} and a spectral mismatch factor of 1.486, measured at a 0.25 V/s scan rate. B) Photocurrent density and power conversion efficiency measured at the maximum power point for a 60s time span.

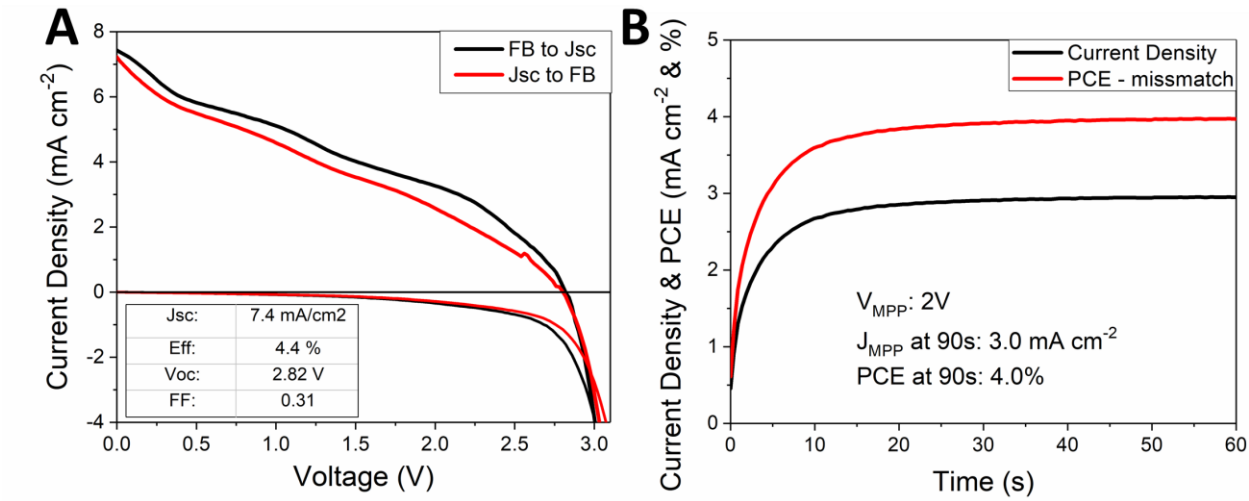

Figure S15 Device performance of a $FA_{0.83}Cs_{0.17}Pb(Br_{0.7}I_{0.3})_3$/$MAPbI_3$/$MAPb_{0.75}Sn_{0.25}I_3$ triple-junction solar cells with the highest open circuit voltage A) Current-voltage characteristic measured under simulated sunlight, with an equivalent irradiance of 98.8 mW cm^{-2} and a spectral mismatch factor of 1.486, measured at a 0.25 V/s scan rate. B) Photocurrent density and power conversion efficiency measured at the maximum power point for a 60s time span.

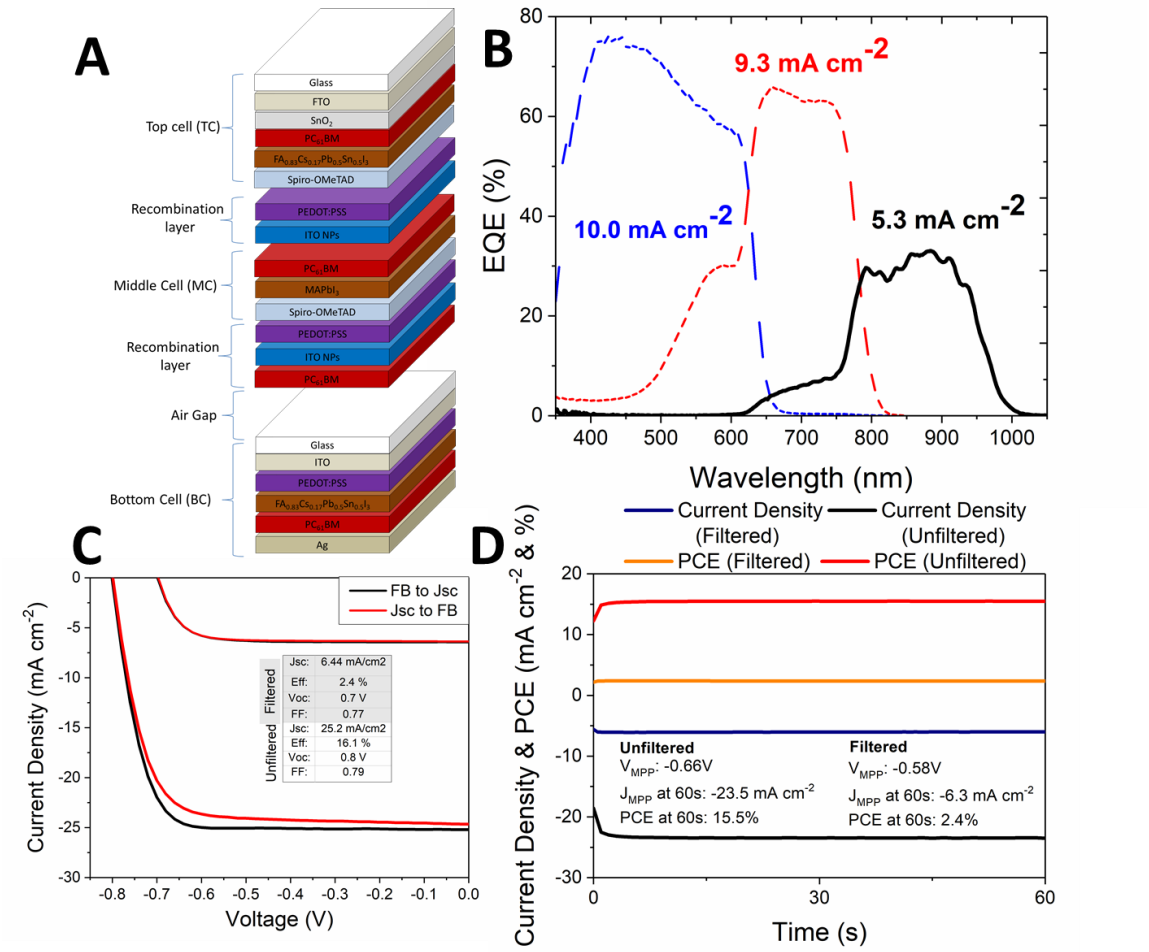

Figure S16 Architecture and device characterization of a $FA_{0.83}Cs_{0.17}Pb_{0.5}Sn_{0.5}I_3$ filtered with a $FA_{0.83}Cs_{0.17}Pb(Br_{0.7}I_{0.3})_3$/$MAPbI_3$ dual-junction solar cells. A) Schematics showing the filtering of the $FA_{0.83}Cs_{0.17}Pb_{0.5}Sn_{0.5}I_3$ perovskite with an all-solution processed perovskite/perovskite two-terminal (2T) $FA_{0.83}Cs_{0.17}Pb(Br_{0.7}I_{0.3})_3$/$MAPbI_3$ tandem perovskite solar cell. B) EQE spectrum for a $FA_{0.83}Cs_{0.17}Pb_{0.5}Sn_{0.5}I_3$ (solid line) filtered with a $FA_{0.83}Cs_{0.17}Pb(Br_{0.7}I_{0.3})_3$/$MAPbI_3$ dual-junction solar cells, and the integrated current density for the tandem perovskite solar cell. We also show alongside, the EQE spectrum for each sub-cell of the $FA_{0.83}Cs_{0.17}Pb(Br_{0.7}I_{0.3})_3$/$MAPbI_3$ tandem perovskite solar cell with an opaque electrode, and the integrated current density for the tandem perovskite solar cell. C) J-V characteristics for the champion a $FA_{0.83}Cs_{0.17}Pb_{0.5}Sn_{0.5}I_3$ unfiltered and filtered with a $FA_{0.83}Cs_{0.17}Pb(Br_{0.7}I_{0.3})_3$/$MAPbI_3$ dual-junction solar cell fabricated, measured at a 0.25 V/s scan rate. C) Photocurrent density and power conversion efficiency measured at the maximum power point for a 60s time span of the $FA_{0.83}Cs_{0.17}Pb_{0.5}Sn_{0.5}I_3$ unfiltered and filtered solar cell. A mismatch factor of 1.486 has been applied to the PCE.

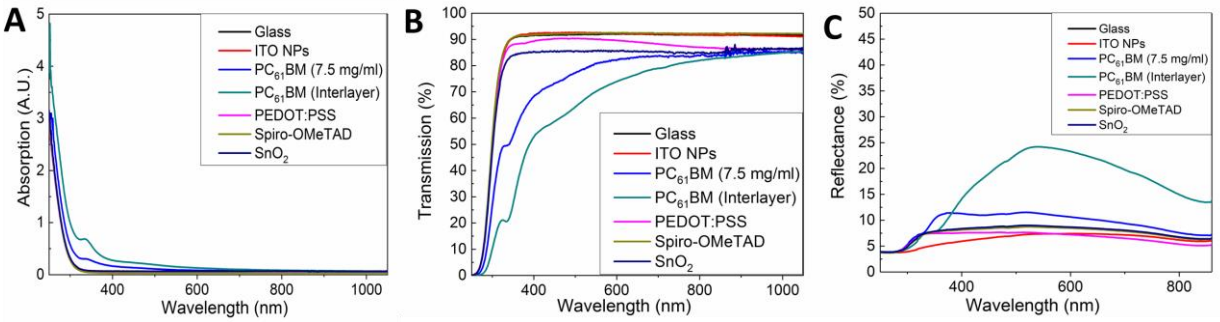

Figure S17 Optical properties of the recombination interlayer and hole and electron accepting layers. A) Absorption measured from 250nm to 1050nm of glass, indium-tin oxide nanoparticles (ITO NPs), phenyl-C61-butyric acid methyl ester ($PC_{61}BM$), phenyl-C61-butyric acid methyl ester ($PC_{61}BM$), poly(3,4-ethylenedioxythiophene) polystyrene sulfonate (PEDOT:PSS), (2,2′,7,7′-tetrakis(N,N′-di-p-methoxyphenylamine)-9,9′-spirobifluorene) (Spiro-OMeTAD). B) Transmission measurement C) Reflectance measurement.

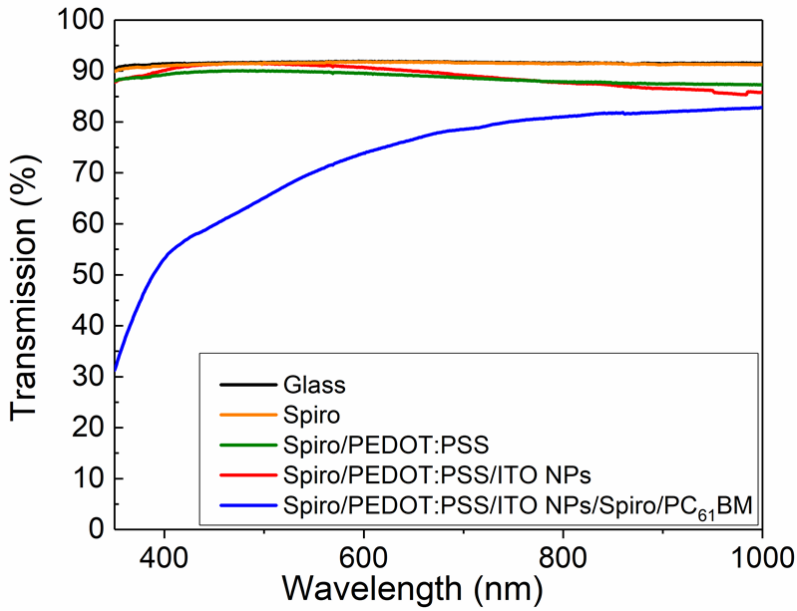

Figure S18 Transmission measurement of sequentially deposition of the hole accepting layer, the recombination interlayer and electron accepting layers.

To calculate the mismatch factor (M) of the tandem solar cell, we employed the give formula[1]:

$$M = \frac{\int E_R(\lambda)\, S_R(\lambda) d\lambda}{\int E_S(\lambda) S_R(\lambda) d\lambda} \; \frac{\min(\int E_S(\lambda)\, S_{top}(\lambda) d\lambda\,, \int E_S(\lambda)\, S_{bot}(\lambda) d\lambda)}{\min(\int E_R(\lambda)\, S_{top}(\lambda) d\lambda\,, \int E_R(\lambda)\, S_{bot}(\lambda) d\lambda)}$$

Where, E_R is the spectral irradiance of the AM1.5G spectrum, S_R is the spectral response of the silicon reference cell, E_S is the relative spectral irradiance of the Abet Class AAB sun 2000 solar simulator, S_{top} is the spectral response of the front cell, S_{bot} is the spectral response of the bot cell.

Architecture	Uncorrected mismatch factor	Mismatch factor after lamp adjusted	Filter for Reference cell

Tandem solar cell	1.050	1.004	KG5
Triple-junction solar cell	1.507	1.486	KG2

Table S1 Table of the calculated mismatch factors for the tandem perovskite solar cell and the triple-junction perovskite solar cell.

Architecture	**Spectral Mismatch Factor**	**Raw efficiency – Uncorrected for Spectral Mismatch**	**Reported efficiency – Corrected for Spectral Mismatch**
Tandem	1.004	15.3%	15.2%
Triple-junction	1.486	9.9%	6.7%

Table S2 Table showing the raw uncorrected efficiency, along with the reported corrected for spectral mismatch for both the tandem and the triple-junction perovskite solar cell.

EXPERIMENTAL SECTION

Front Cell (TC) Fabrication: Glass/FTO/SnO_2/$PC_{61}BM$/$FA_{0.83}Cs_{0.17}Pb(Br_{0.7}I_{0.3})_3$/Spiro-OMeTAD
Substrate Preparation: Devices were fabricated on fluorine-doped tin oxide (FTO) coated glass (Pilkington, 15Ω □$^{-1}$). Initially, FTO was removed at specific regions where the anode contact will be deposited. This FTO etching was done using a 2M HCl and zinc powder. Substrates were then cleaned with Hellmanex detergent and rinsed with water. Finally, the substrates were then cleaned sequentially in acetone, isopropyl alcohol (IPA), and dried with a compressed air gun.

Tin Oxide (SnO_2) layer fabrication: Immediately prior to spin coating, we prepared a SnO_2 precursor solution comprised of 17.5mg ml^{-1} tin(IV) chloride pentahydrate ($SnCl_4 \cdot 5H_2O$) (Sigma-Aldrich) dissolved in anhydrous 2-propanol (IPA). The solution was spin-coated in nitrogen at 3000 rpm for 30 s, with a ramp of 200 rpm/s. The substrates were then dried in nitrogen at 100 °C for 10 min. A subsequent annealing step was done in air at 180 °C for 90 min.

$PC_{61}BM$ layer fabrication: A Phenyl-C61-butyric acid methyl ester ($PC_{61}BM$) precursor solution was prepared by dissolving a 7.5 mg ml^{-1} $PC_{61}BM$ (99%, solenne) in anhydrous chlorobenzene (CB) (Sigma). We doped the $PC_{61}BM$ using dihydro-1H-benzoimidazol-2-yl (N-DBI) derivatives, specifically 3-dimethyl-2-phenyl-2,3-dihydro-1H-benzoimidazole (N-DMBI).[2–7] We doped the $PC_{61}BM$ precursor solution with N-DMBI at a 0.25% wt%. This solution was then filtered using a 0.45 □m PTFE filter. We spin coated this solution in a nitrogen-filled glovebox at 2000 rpm for 20s with a ramp rate of 1000 rpm/s, and annealed the substrate at 80 °C for 10 min.

FAI synthesis: Formamidinium iodide (FAI) was synthesized by dissolving formamidine acetate salt (99%, Sigma-Aldrich) in a 1.5x molar excess of hydriodic acid (HI), 57 wt. % in H_2O, distilled, stabilized, 99.95% (Sigma-Aldrich). After addition of acid the solution was left stirring for 10 minutes at 50 °C. Upon drying in a large glass dish at 100°C for 2h, a yellow-white powder was formed. This was then washed three times with diethyl ether. The power was later dissolved in anhydrous ethanol (99.5%, Sigma-Aldrich) and heated at 120 °C in a N_2-rich atmosphere to obtain a supersaturated solution. Once fully dissolved, the solution was then slowly cooled to room temperature in a N_2-rich atmosphere, until recrystallization occured. The recrystallization process formed white flake-like crystals. The solution was then placed and in a refrigerator at 4 °C, after which it was transferred to a freezer for further crystallization. The powder was later washed with diethyl ether three times. Finally, the powder was dried overnight in a vacuum oven at 50 °C.

$FA_{0.83}Cs_{0.17}Pb(Br_{0.7}I_{0.3})_3$ with 2% K additive perovskite precursor solution preparation: FA/Cs (formamidinium/Cs) with 2% K additive perovskite solutions were prepared by dissolving the precursor salts in anhydrous N,N-dimethylformamide (DMF) to obtain a stoichiometric solution with the desired $FA_{0.83}Cs_{0.17}Pb(Br_{0.7}I_{0.3})_3$ composition and 2% K additive using a molar ratio of 30% to 70% KI to KBr. The precursor solution was prepared using the following precursor salts: formamidinium iodide (FAI), cesium iodide (CsI) (99.9%, Alfa Aesar), lead iodide (PbI_2) (99%, Sigma-Aldrich), lead bromide ($PbBr_2$) (98%, Alfa Aesar), potassium iodide (KI) (99%, Sigma-Aldrich), potassium bromide (99%, KBr) (Sigma-Aldrich). 27.2 µl/ml of hydroiodic acid (HI) (57 wt. % in H_2O, distilled, stabilized, 99.95%, Sigma-Aldrich) and 54.8 µl/ml of hydrobromic (HBr) (48 wt. % in H_2O) was added to 1ml of 0.75 M precursor solutions. After the addition of the acids, the perovskite precursor solution was aged for 2 days under a nitrogen atmosphere.

$FA_{0.83}Cs_{0.17}Pb(Br_{0.7}I_{0.3})_3$ perovskite layer preparation: This aged precursor perovskite solution was spin-coated in a nitrogen-filled glovebox at 1200 rpm for 45s with a 600 rpm/s ramp rate. The films were dried inside a N_2 glovebox on a hot plate at a temperature of 70 °C for 1 minute. The films were then annealed in an oven in an air atmosphere at 185°C for 90 minutes. During this annealing process, the samples were covered with a large glass container to prevent dust contamination.

Spiro-OMeTAD hole-transporting layer fabrication: The electron-blocking layer was deposited with a 72.5mg/ml of 2,2',7,7'-tetrakis-(N,N-di-p-methoxyphenylamine)9,9'-spirobifluorene (spiro-OMeTAD) (Lumtec) solution in chlorobenzene. Additives of 38µl of lithium bis(trifluoromethanesulfonyl)imide (170mg/mL in 1-butanol solution) per 1ml of spiro-OMeTAD solution and 21µl of 4-tert-butylpyridine (TBP) per 1mL of spiro-OMeTAD solution. The samples were left to oxidize in a desiccator for 24h. Spin-coating was carried out in a nitrogen-filled glovebox at 2000rpm for 20s with a ramp rate of 1000 rpm/s.

Recombination Interlayer layer fabrication (for both TC/MC and MC/BC): PEDOT:PSS/ITO NPs
The interlayer is fabricated using both PEDOT:PSS (PH 1000) in water (Heraeus Clevios) and indium-tin oxide, 30 wt. % in isopropanol (IPA), (ITO) <100nm nanoparticles (NPs) dispersion (Sigma), as precursor solutions.
We first deposit a thin layer of PEDOT:PSS directly on top of the existing spiro-OMeTAD layer. The PEDOT:PSS precursor solution was prepared immediately prior to spin coating, by diluting PEDOT:PSS (PH 1000) in anhydrous 2-propanol (IPA) at a volume ratio of 1 to 1.5 (PEDOT:PSS to IPA) and then filtered with a 2.7 □m GF/D membrane filter (Whatman). The substrates were preheated at 80 °C, and we then dynamically spin coated the diluted PEDOT:PSS solution, in a dry air atmosphere <10% relative humidity (RHM), at a speed of 6000 rpm for 20 s, and then annealed for at 80 °C for 10 min.
We then deposited the ITO NPs layer. We prepared the ITO NPs precursor solution by diluting the 30 wt. % in IPA down to 1 wt. % in IPA. The diluted solution was sonicated, in a sonication bath, for 15 m prior to deposition. We dynamically spin coated the diluted ITO NPs solution, in a dry air atmosphere <10% relative humidity (RHM), at a speed of 6000 rpm for 20 s, and then annealed for at 80 °C for 10 m.

Middle Cell (MC) Fabrication: $PC_{61}BM/MAPbI_3$/Spiro-OMeTAD
$PC_{61}BM$ layer fabrication: A Phenyl-C61-butyric acid methyl ester ($PC_{61}BM$) precursor solution was prepared by dissolving a 30 mg ml^{-1} $PC_{61}BM$ (99%, solenne) in a mixture of anhydrous chlorobenzene (CB) (sigma) and anhydrous chloroform (CF) solvents. The solvents were mixed at a volume ratio of 2 to 1, CB to CF. We doped the $PC_{61}BM$ using dihydro-1H-benzoimidazol-2-yl (N-DBI) derivatives, specifically 3-dimethyl-2-phenyl-2,3-dihydro-1H-benzoimidazole (N-DMBI).[2–7] We doped the $PC_{61}BM$ precursor solution with N-DMBI at a 0.25 wt%. This solution was then filtered using a 0.45 □m PTFE filter. The substrates were preheated at 80 °C, we then dynamically spin coated this solution in a dry air atmosphere <10% relative humidity (RHM) at 4000 rpm for 20s, and annealed the substrate at 80 °C for 10 min.

ACN/MA $MAPbI_3$ perovskite precursor solution preparation:
In this work, we found that controlling the MA content in the acetonitrile(CH_3CN)/methylamine(CH_3NH_2) (ACN/MA) $MAPbI_3$ solution resulted in better tandem performance with higher reproducibility. Excess MA in the ACN/MA $MAPbI_3$ solution can potentially percolate through pinholes of thin imperfect interlayers, thus partially or completely dissolving the underlying junction. Thus, solutions with the minimal amount of MA required to dissolve the perovskite were employed. Controlling the MA content in the solution can potentially be done by controlling the MA flow rate and stirring speed, however, precisely controlling these parameters was sometimes challenging. Instead, we prepared two ACN $MAPbI_3$ dispersions, one with excess MA content resulting in a full ACN/MA $MAPbI_3$ solution, and another ACN $MAPbI_3$ dispersion without any MA. Immediately prior to spin coating, we slowly add the ACN/MA $MAPbI_3$ with excess MA to the ACN $MAPbI_3$ dispersion until this dispersion is fully dissolved, and becomes a full solution. The resulting solution is an ACN/MA $MAPbI_3$ solution at its critical solubility point. The preparations of the ACN/MA $MAPbI_3$ solution and the ACN $MAPbI_3$ dispersion are described below.
The ACN $MAPbI_3$ perovskite precursor solution without any MA was prepared, under nitrogen, using precursor salts methylammonium iodide (MAI) (Dyesol) and lead iodide (PbI_2) (TCI) added into anhydrous acetonitrile (ACN) (Sigma Aldrich) at a concentration of 1.03 M for MAI and 1 M for PbI_2, resulting in a non-stoichiometric solution (1.03:1 MAI:PbI_2). This solution was then sonicated, in a sonication bath, for 1 h in order to fully react the MAI with the PbI_2, a black perovskite dispersion is then seen at the bottom of the ACN filled vial.

The ACN/MA $MAPbI_3$ perovskite precursor solution was prepared using an adapted method described by Noel et al.[8] We first prepare an ACN/MA $MAPbI_3$ perovskite precursor solution with the identical preparation method as described above. In order to dissolve the perovskite in ACN, a solution of methylamine (MA) in ethanol (Sigma Aldrich, 33 wt%) was placed into an aerator which was kept in an ice bath. Nitrogen was then bubbled into the solution, thus degassing the solution of MA. The MA gas which was produced was then passed through a drying tube filled with a desiccant (Drietire and CaO). The gas was bubbled into the black dispersion, while vigorously stirring the ACN/MA $MAPbI_3$ dispersion using a large magnetic stir bar at a speed of approximately 700 rpm. The dispersion was bubbled for 15 minutes, which resulted in a full dissolution of the black perovskite particles, resulting in a clear, light yellow solution. We note this solution has an "excess" amount of MA in the ACN/MA $MAPbI_3$ solution.

ACN/MA $MAPbI_3$ perovskite layer preparation: The ACN/MA $MAPbI_3$ precursor perovskite solution (at it's critical solubility point) is immediately dynamically spin coated in a dry air atmosphere <10% relative humidity (RHM) at 5000 rpm for 20s. A post treatment of methylammonium chloride (MACl) was then carried out by dynamically spincoating at 6000 rpm for 20s a 50 µl of MACl (Alfa Aesar, 2 mg/ml in isopropanol). The films were then annealed in an oven in an air atmosphere at 80 °C for 90 minutes. During this annealing process, the samples were covered with a large glass container to prevent dust contamination.

ACN/MA $MAPbI_3$ perovskite layer preparation with FAI/CsBr post-treatment: The ACN/MA $MAPbI_3$ precursor perovskite solution (at it's critical solubility point) is immediately dynamically spin coated in a dry air atmosphere <10% relative humidity (RHM) at 5000 rpm for 20s. A formamidinium iodide (FAI) and cesium bromide (CsBr) post-treatment was then carried out by dynamically spincoating a 50 µl of a 0.2M solution of FAI/CsBr (83/17, molar ratio) dissolved in methanol (MeOH), at 6000 rpm for 20s. The films are annealed for 10 minutes at 80 °C. After cooling the film to room temperature, a 200 µl isopropanol solution was dynamically spin coated at 6000 rpm for 20s, to remove excess cations. The films were then annealed in an oven in an air atmosphere at 80 °C for 90 minutes. During this annealing process, the samples were covered with a large glass container to prevent dust contamination.
Spiro-OMeTAD hole-transporting layer fabrication: The electron-blocking layer was deposited by dynamically spin coating a 85mg/ml of 2,2',7,7'-tetrakis-(N,N-di-p-methoxyphenylamine)9,9'-spirobifluorene (spiro-OMeTAD) (Lumtec) solution in chlorobenzene. Additives of 20µl of lithium bis(trifluoromethanesulfonyl)imide (520mg/mL in acetonitrile solution) per 1ml of spiro-

OMeTAD solution and 33µl of 4-tert-butylpyridine (*t*BP) per 1mL of spiro-OMeTAD solution. Spin-coating was done dynamically and carried out in a dry air atmosphere <10% relative humidity (RHM) at 2000 rpm for 30s. The samples were left to oxidize in a desiccator for 24h.

Rear Cell (BC) Fabrication: $PC_{61}BM/MAPb_{0.75}Sn_{0.25}I_3/Spiro(TFSI)_2$

$PC_{61}BM$ layer fabrication: A Phenyl-C61-butyric acid methyl ester ($PC_{61}BM$) precursor solution was prepared by dissolving a 30 mg ml^{-1} $PC_{61}BM$ (99%, solenne) in a mixture of anhydrous chlorobenzene (CB) (sigma) and anhydrous chloroform (CF) solvents. The solvents were mixed at a volume ratio of 2 to 1, CB to CF. We doped the $PC_{61}BM$ using dihydro-1H-benzoimidazol-2-yl (N-DBI) derivatives, specifically 3-dimethyl-2-phenyl-2,3-dihydro-1H-benzoimidazole (N-DMBI).[2–7] We doped the $PC_{61}BM$ precursor solution with N-DMBI at a 0.25% wt%. This solution was then filtered using a 0.45 □m PTFE filter. The substrates were preheated at 80 °C, we then dynamically spin coated this solution in a dry air atmosphere <10% relative humidity (RHM) at 4000 rpm for 20s, and annealed the substrate at 80 °C for 10 min.

ACN/MA $MAPb_{0.75}Sn_{0.25}I_3$ perovskite precursor solution preparation:

To obtain a mixed-metal ACN/MA $MAPb_{0.75}Sn_{0.25}I_3$ perovskite precursor solution, we mixed an ACN/MA $MAPbI_3$ with an ACN $MAPb_{0.5}Sn_{0.5}I_3$ (without any MA) at a 1:1 volume ratio, resulting in an ACN/MA $MAPb_{0.75}Sn_{0.25}I_3$.

The ACN/MA $MAPb_{0.5}Sn_{0.5}I_3$ solution perovskite precursor solution, without any MA was prepared, under nitrogen, using precursor salts methylammonium iodide (MAI) (Dyesol), lead iodide (PbI_2) (TCI), and anhydrous tin iodide (SnI_2) beads (TCI) added into anhydrous acetonitrile (ACN) (Sigma Aldrich) at a concentration of 0.8 M for MAI, 0.46 M for PbI_2 and 0.46 M for SnI_2, resulting in a non-stoichiometric solution with 15% excess metal salts (1:1.15 MAI:PbI_2+SnI_2). This solution was then stirred under nitrogen at 70 °C for 1h, in order to fully react the MAI with the mixed metals, a black perovskite dispersion is then seen at the bottom of the ACN filled vial.

The ACN/MA $MAPbI_3$ perovskite precursor solution was prepared using an adapted method described by Noel et al.[8] We first prepare a ACN/MA $MAPbI_3$ perovskite precursor solution at a 0.8 M for MAI and 0.46 M for PbI_2, resulting in a non-stoichiometric solution with 15% excess metal salts (1:1.15 MAI:PbI_2). In order to dissolve the perovskite in ACN, a solution of methylamine (MA) in water H_2O (Sigma Aldrich, 40 wt%) was placed into an aerator which was kept in an ice bath. Nitrogen was then bubbled into the solution, thus degassing the solution of MA. The MA gas which was produced was then passed through a drying tube filled with a desiccant (Drietire and CaO). The gas was bubbled into the black dispersion, while vigorously stirring the ACN/MA $MAPbI_3$ dispersion using a large magnetic stir bar at a speed of approximately 700 rpm. The dispersion was bubbled for 15 minutes, which resulted in a full dissolution of the black perovskite particles, resulting in a clear, light yellow solution. We note this solution has an "excess" amount of MA in the ACN/MA $MAPbI_3$ solution. The solution was then stored in nitrogen for approximately 3 h with activated 3 Å molecular sieves to remove any H_2O that was introduced during the MA bubbling process.

ACN/MA $MAPb_{0.75}Sn_{0.25}I_3$ perovskite layer: This precursor perovskite solution is immediately dynamically spin coated in a nitrogen glovebox at 5000 rpm for 20s. A second subsequent spin coating step was used to deposit a methylammonium chloride (MACl) post treatment. A 2 mg ml^{-1} solution of MACl in IPA was dynamically spin coated at 6000rpm for 20s. The films were then annealed in nitrogen at 80°C for 90 minutes.

Spiro(TFSI)$_2$ synthesis: The Spiro(TFSI)$_2$ hole-transporting layer used for the $MAPb_{0.75}Sn_{0.25}I_3$ perovskite was prepared using an adapted method described by Nguyen et al.[9] We first dissolved 2,2',7,7'-tetrakis-(N,N-di-p-methoxyphenylamine)9,9'-spirobifluorene (spiro-OMeTAD) (Lumtec) solution in chlorobenzene (CB) at a 2 mg ml^{-1} concentration. Separately, we dissolved the Silver(I) bis(trifluoromethanesulfonyl)imide (Ag-TFSI) in methanol at a 100 mg ml^{-1}. We slowly mixed identical volumes of both solutions together, while stirring. The final molar ratio is 1 to 0.95 (spiro-OMeTAD to Ag-TFSI). We then left the mixed solution stirring overnight. We filtered the solution with a 0.2 □m PTFE filter to remove the Ag colloids. We used a rotary evaporation to remove CB until approximately 5% of the original volume is left. We then added toluene to the remaining flask at a volume of 50% of the initial CB volume. We placed the solution in a refrigerator for 24h, where a fine black powder precipitated. Once, the black powder fully settled, we removed excess toluene using a glass frit filter. We washed the powder with a cold 4 °C toluene. Once the powder was dry, we prepared a 20 mg ml^{-1} in methanol solution. This black powder should not have low solubility in methanol, which starts the precipitation process. We refrigerated the solution at 4 °C overnight. The black powder collected at the bottom of the vial. We removed the excess toluene using a glass frit filter, and washed with 4 °C methanol. Once dry, we collected and weighed the Spiro(TFSI)$_2$ powder.

Spiro-OMeTAD doped with 10 wt.% Spiro(TFSI)$_2$ hole-transporting layer fabrication: The electron-blocking layer was deposited by dynamically spin coating a spiro(TFSI)$_2$ doped spiro-OMeTAD at 2000 rpm for 30s in a nitrogen glovebox. This precursor solution was prepared with a 72.5 mg ml^{-1} wt.% spiro solution composed of a 7.25 mg ml^{-1} Spiro(TFSI)$_2$ and a 65.25 mg ml^{-1} 2,2',7,7'-tetrakis-(N,N-di-p-methoxyphenylamine)9,9'-spirobifluorene (spiro-OMeTAD) (Lumtec) solution in chlorobenzene. No additives were added to the spiro-OMeTAD solution.

Rear Cell (BC) Fabrication: PEDOT:PSS/$FA_{0.83}Cs_{0.17}Pb_{0.5}Sn_{0.5}I_3$/$PC_{61}BM$/BCP

$FA_{0.83}Cs_{0.17}Pb_{0.5}Sn_{0.5}I_3$ perovskite precursor preparation: A stoichiometric solution of 1.2 M $FA_{0.83}Cs_{0.17}Pb_{0.5}Sn_{0.5}I_3$ was prepared in a nitrogen atmosphere by dissolving FAI (Dyesol), CsI (99.9%, Alfa Aesar), PbI_2 (99.999%, Alfa Aesar), and SnI_2 (99.999%, Alfa Aesar) in a mixed solvent of 4:1 DMF:DMSO by volume. Also dissolved in the solution is 60 mM tin (II) fluoride (SnF_2, 99%, Sigma Aldrich) and 36 mM lead (II) thiocyanate (99.5%, Sigma Aldrich).

Device preparation: Patterned indium tin oxide (ITO) substrates were cleaned by sequentially rinsing in acetone and IPA. Once dried, the substrates were cleaned with an O_2-plasma for ten minutes. Immediately following plasma treatment, a PEDOT:PSS solution (PVP AI 4083, Heraeus, in a 1:2 volume ratio with methanol) was spincoated in ambient conditions at 4 krpm for 30 s, followed by annealing at 150 °C in ambient for 10 minutes. The devices were immediately transferred to a N_2 glovebox. Just prior to fabricating the perovskite film the PEDOT:PSS coated ITO substrates were annealed again at 120 °C for 10 minutes. The perovskite film was fabricated by spincoating the solution at 3.6 krpm for 14 s with a 6 s ramp. At 13 s after the start of the spincoating program, 200 μL of anisole was dispensed onto the spinning substrate. Once spincoating is finished, a stream of N_2 was applied to the film for 15 s and then immediately annealed at 120 °C for 10 minutes. The $PC_{61}BM$ layer was produced by dynamically spincoating 50 uL of a hot solution (90°C) of $PC_{61}BM$ (20 mg/mL dissolved in a mixed solvent of 3:1 chlorobenzene:1,2-dichlorobenzene by volume) at 2 krpm for 30 s and subsequently annealed at 90°C for 2 minutes. Once cooled to room temperature, 70 μL of a 0.5 mg/mL solution of bathocuproin (BCP, 98%, Alfa Aesar) was dynamically spincoated at 4 krpm for 20 s.

Electrode: A 100 nm silver or gold electrode was thermally evaporated under vacuum of $\approx 10^{-6}$ Torr, at a rate of ≈ 0.2 nm·s^{-1}.

Solar cell characterization: The current density–voltage (J-V) curves were measured (2400 Series SourceMeter, Keithley Instruments) under simulated AM 1.5 sunlight at approximately 100 mWcm^{-2} irradiance generated by an Abet Class AAB sun 2000 simulator, with the intensity calibrated with an NREL calibrated KG5 filtered Si reference cell. For single junctions, the mismatch factor was calculated to be less than 1%. For multi-junctions, the mismatch factor was calculated for each junction and PCE were adjusted accordingly. The active area of the solar cell is 0.0919 cm^{-2}. The forward J–V scans were measured from forward bias (FB) to short circuit (SC) and the backward scans were from short circuit to forward bias, both at a scan rate of 0.25V s^{-1}. A stabilization time of 5 seconds under 1 sun illumination and forward bias of 0.3V above the expected V_{OC} was done prior to scanning.

External quantum efficiency (EQE) characterization: The multi-junction EQEs were measured by optically biasing the sub-cells that are not being measured with a 3W 470-475 nm LED and a 3W 730-740 nm LED, for the TC and for the BC, respectively. A negative bias equal to V_{oc} of the sub-junction that is being optically biased was applied to the tandem during the measurement. This allows us to measure the response of the tandem in short-circuit condition.

Transient photoconductivity: The Nd:YAG laser excitation source tuned to 470 nm and pumped at 10 Hz with 3.7 ns pulses is used at the range of fluences to have various charge carrier density as described in the main text. This pulse light is illuminated across the entire sample area to evenly excite the film. A bias of 24 V is applied across the in-plane (lateral) electrodes. Here, since the contact resistance between perovskite film and Au electrode is fairly small compared to sample resistance, we employ a two-point probe conductivity measurement. A variable resistor is in series with sample in the circuit to always be <1% of the sample resistance. We monitored the voltage drop across a variable resistance, placed in series with the sample, using a 1MΩ input resistance oscilloscope to determine the potential drop across the two in-plane Au electrodes (4 mm channel to channel distance) in the sample. Perovskite film is scribed to have 5mm channel width, and coated with inert 200nm PMMA. Transient photoconductivity ($\sigma_{Transient-Photo}$) was calculated by the equation, $\sigma_{Transient-Photo} = \frac{V_r}{R_r \times (V_{bias} - V_r)} \times \frac{l}{w \times t}$ where, V_r is voltage drop across the resistor, R_r is variable resistor, V_{bias} is bias voltage, l is channel-channel length, w is channel width, and t is film thickness.

Modeling:

Overview

We modelled the optical properties of the stack using a generalized transfer matrix method (TMM).[10] All the calculations were done in Python with heavy use of the NumPy and SciPy libraries. The wavelength dependent complex refractive index, the layer thicknesses and the incidence angle were fed as input.

The TMM model outputs the electric field distribution in the stack. This was used to calculate Transmittance $T(E)$, Reflectance $R(E)$ and the absorption $A(E)$ in each layer. The short circuit current of each sub-cell was then determined by assuming the internal quantum efficiency to be unity:

$$J_{SC} = q \int_0^{\infty} A(E) \cdot \phi_{AM1.5}(E) \cdot dE$$

Here, $\phi_{AM1.5}(E)$ is the photon flux from the AM1.5 spectrum.

The JV curve from each sub-cell was obtained by combining this modelled J_{SC} with the electrical characteristics of state-of-art single junction cells. To do this, we parametrized the JV curves of state-of-the-art single junctions as per the single diode equivalent model:

$$J(V) = J_{sun} - J_0 \left(e^{\frac{V + J(V)R_S}{nV_T}} - 1 \right) - \frac{V + J(V)R_S}{R_{SH}}$$

Where n, V_T, R_S, J_0 and R_{SH} are respectively the electron charge, thermal voltage at 300K, series resistance, dark current, and shunt resistance. The JV curve of each multi-junction sub-cell is modelled by replacing J_{sun} in the fitted equation with the J_{SC} calculated from the multijunction stack. As the correlation between J_{sun} and other fitting parameters is negligible, we can be sure that J_{sun} can be changed without changing other parameters. The approach of Jain et al.[11] was used to solve the single diode model using the Lambert W function. After calculating the JV curves of all sub-cells, we combined them to obtain the multi-junction JV curve.[12] The maximum point is calculated from this combined JV curve.

Inputs for the Optical and Electrical Models

The refractive indices for ITO[13], FTO[14], PEDOT:PSS[15], PCBM[16], Spiro-OMeTAD[17], Ag[18], $MA_{0.4}FA_{0.6}Sn_{0.6}Pb_{0.4}I_3$[19] and $MAPbI_3$ [20] were taken from the literature. The extinction co-efficient k of $FA_{0.83}Cs_{0.17}Pb(Br_{0.7}I_{0.3})_3$ was obtained by measuring the transmittance T and the reflectance R of a thin film of thickness t on glass and using the relations:

$$\alpha = \frac{4\pi k}{\lambda}$$

$$\frac{T}{1-R} = e^{\alpha t}$$

Once $k(\lambda)$ was obtained, we parametrized it in terms of Lorentz oscillators to get an analytical representation, which was transformed into the refractive index $n(\lambda)$ via the Kramers-Kronig transform:

$$n(\lambda) = 1 + \frac{2}{\pi}\int_0^\infty \frac{E'k(E)}{E'^2 - E^2}dE'$$

The electrical characteristics for the $MAPbI_3$ [21]and the $MAPb_{0.75}Sn_{0.25}I_3$[22] are taken from best reported cells of same or similar class in the literature. For the $FA_{0.83}Cs_{0.17}Pb(Br_{0.7}I_{0.3})_3$ sub-cell, we use the JV curve of our best $FA_{0.83}Cs_{0.17}Pb(Br_{0.7}I_{0.3})_3$ single junction cell (Figure S3).

To account for the ITO nanoparticles being embedded in PCBM, we model its refractive index as a Bruggeman Effective Medium with 75% ITO and 25% PCBM. The refractive index of this effective medium is calculated by solving:

$$\frac{f_{ITO}(n_{ITO}^2 - n^2)}{(n_{ITO}^2 + 2n^2)} = \frac{(1-f_{FTO})(n_{PCBM}^2 - n^2)}{(n_{PCBM}^2 + 2n^2)}$$

Where n_{ITO}, n_{PCBM} and f_{ITO} are respectively the complex refractive index of ITO, complex refractive index of PCBM and the fraction of ITO in the effective medium.

Tandem Simulation

$FA_{0.83}Cs_{0.17}Pb(Br_{0.7}I_{0.3})_3$/$MAPbI_3$ simulation - Figure A,B

The thicknesses used in the optical model are obtained from an SEM cross section of the tandem. The electrical characteristics of $FA_{0.83}Cs_{0.17}Pb(Br_{0.7}I_{0.3})_3$ and $MAPbI_3$ presented are extracted from our own single junction devices (FigureS3). The dotted JV models the performance assuming the $MAPbI_3$ performs as well as the best ACN processed $MAPbI_3$ cell in literature.

Layer	**Thickness**
Glass	2.2mm
ITO	350nm
SnO_2	40nm
PCBM	10nm
$FA_{0.83}Cs_{0.17}Pb(Br_{0.7}I_{0.3})_3$	350nm
Spiro-OMeTAD	250nm

PEDOT:PSS	15nm
ITO Nanoparticles:PCBM 75:25 Effective Medium	50nm
PCBM	80nm
$MAPbI_3$	530nm
Spiro-OMeTAD	180nm
Ag	100nm

$FA_{0.83}Cs_{0.17}Pb(Br_{0.7}I_{0.3})_3$/$MAPbI_3$ (optimized) - Figure C,D

We cap the thicknesses of the non-perovskite layers at 50nm. We add a MgF_2 anti-reflecting coating. We optimize the thicknesses of the perovskite layers and the anti-reflecting coating using a differential evolution algorithm to maximize the limiting current.

The electrical characteristics of the $FA_{0.83}Cs_{0.17}Pb(Br_{0.7}I_{0.3})_3$ are from our own device (Fig S3). The characteristics of the $MAPbI_3$ are from the best cell $MAPbI_3$ in literature.[23] The dotted JV curve models the performance of the tandem assuming the front cell electrically performs as well as current state-of-the-art in Perovskites. We follow the approach of Hörantner et al [19] for this, and assume $EQE_{EL} = 0.01$, $R_S = 4 \cdot 10^{-2}\ \Omega\ cm^2$ and $R_{SH} = 10M\Omega\ cm^2$.

Layer	Thickness
MgF_2	Search space: 10-500nm Optimized: 104nm
Glass	2.2mm
FTO	50nm
SnO_2	40nm
PCBM	10nm
$FA_{0.83}Cs_{0.17}Pb(Br_{0.7}I_{0.3})_3$	Search space: 100-1500nm Optimized: 381nm
Spiro-OMeTAD	50nm
PEDOT:PSS	15nm
ITO Nanoparticles: PCBM 75:25 Effective Medium	50nm
PCBM	50nm
$MAPbI_3$	Search space: 100-1500nm Optimized: 1382nm
Spiro-OMeTAD	50nm
Ag	100nm

$FA_{0.83}Cs_{0.17}Pb(Br_{0.7}I_{0.3})_3$/$MAPbI_3$/$MA_{0.4}FA_{0.6}Pb_{0.4}Sn_{0.6}I_3$ triple-junction simulation (optimized)

The calculations for figures E,F are performed exactly as for figures C,D. For the dotted triple junction JV curve, both the front and rear cells are modelled as current state-of-the-art perovskite cells.

Layer	**Thickness**
MgF_2	Search space: 10-500nm Optimized: 92.8nm
Glass	2.2mm
FTO	50nm
SnO_2	40nm
PCBM	10nm
$FA_{0.83}Cs_{0.17}Pb(Br_{0.7}I_{0.3})_3$	Search space: 100-1500nm Optimized: 296.7nm
Spiro-OMeTAD	50nm
PEDOT:PSS	15nm
ITO Nanoparticles:PCBM 75:25 Effective Medium	50nm
PCBM	50nm
$MAPbI_3$	Search space: 100-1500nm Optimized: 583.3
Spiro-OMeTAD	50nm
PEDOT:PSS	15nm
ITO Nanoparticles:PCBM 75:25 Effective Medium	50nm
PCBM	50nm
$MA_{0.4}FA_{0.6}Pb_{0.4}Sn_{0.6}I_3$	Search space: 100-1500nm Optimized: 1382.4
Spiro-OMeTAD	50nm
Ag	100nm

References

[1] Snaith HJ. How should you measure your excitonic solar cells? Energy Environ Sci 2012;5:6513. doi:10.1039/c2ee03429h.

[2] Rossbauer S, Müller C, Anthopoulos TD. Comparative Study of the N-Type Doping Efficiency in Solution-processed Fullerenes and Fullerene Derivatives. Adv Funct Mater 2014;24:n/a-n/a. doi:10.1002/adfm.201401842.

[3] Wang Z, McMeekin DP, Sakai N, van Reenen S, Wojciechowski K, Patel JB, et al. Efficient and Air-Stable Mixed-Cation Lead Mixed-Halide Perovskite Solar Cells with n-Doped Organic Electron Extraction Layers. Adv Mater 2017;29:1604186. doi:10.1002/adma.201604186.

[4] Kim SS, Bae S, Jo WH. Performance enhancement of planar heterojunction perovskite solar cells by n-doping of the electron transporting layer. Chem Commun 2015;51:17413–6. doi:10.1039/C5CC05253J.

[5] Wei P, Menke T, Naab BD, Leo K, Riede M, Bao Z. 2-(2-Methoxyphenyl)-1,3-dimethyl-1 *H* -benzoimidazol-3-ium Iodide as a New Air-Stable n-Type Dopant for Vacuum-Processed Organic Semiconductor Thin Films. J Am Chem Soc 2012;134:3999–4002.

doi:10.1021/ja211382x.
[6] Naab BD, Guo S, Olthof S, Evans EGB, Wei P, Millhauser GL, et al. Mechanistic Study on the Solution-Phase n-Doping of 1,3-Dimethyl-2-aryl-2,3-dihydro-1 *H* -benzoimidazole Derivatives. J Am Chem Soc 2013;135:15018–25. doi:10.1021/ja403906d.
[7] Wei P, Oh JH, Dong G, Bao Z. Use of a 1 *H* -Benzoimidazole Derivative as an *n* -Type Dopant and To Enable Air-Stable Solution-Processed *n* -Channel Organic Thin-Film Transistors. J Am Chem Soc 2010;132:8852–3. doi:10.1021/ja103173m.
[8] Noel NK, Habisreutinger SN, Wenger B, Klug MT, Hörantner MT, Johnston MB, et al. A low viscosity, low boiling point, clean solvent system for the rapid crystallisation of highly specular perovskite films. Energy Environ Sci 2017;10:145–52. doi:10.1039/C6EE02373H.
[9] Nguyen WH, Bailie CD, Unger EL, McGehee MD. Enhancing the Hole-Conductivity of Spiro-OMeTAD without Oxygen or Lithium Salts by Using Spiro(TFSI) $_2$ in Perovskite and Dye-Sensitized Solar Cells. J Am Chem Soc 2014;136:10996–1001. doi:10.1021/ja504539w.
[10] Centurioni E. Generalized matrix method for calculation of internal light energy flux in mixed coherent and incoherent multilayers. Appl Opt 2005;44:7532. doi:10.1364/AO.44.007532.
[11] Jain A, Kapoor A. Exact analytical solutions of the parameters of real solar cells using Lambert W -function. Sol Energy Mater Sol Cells 2004;81:269–77. doi:10.1016/j.solmat.2003.11.018.
[12] Hadipour A, de Boer B, Blom PWM. Device operation of organic tandem solar cells. Org Electron 2008;9:617–24. doi:10.1016/J.ORGEL.2008.03.009.
[13] K??nig TAF, Ledin PA, Kerszulis J, Mahmoud MA, El-Sayed MA, Reynolds JR, et al. Electrically tunable plasmonic behavior of nanocube-polymer nanomaterials induced by a redox-active electrochromic polymer. ACS Nano 2014;8:6182–92. doi:10.1021/nn501601e.
[14] Ball JM, Stranks SD, Hörantner MT, Hüttner S, Zhang W, Crossland EJW, et al. Optical properties and limiting photocurrent of thin-film perovskite solar cells. Energy Environ Sci 2015;8:602–9. doi:10.1039/C4EE03224A.
[15] Shi D, Adinolfi V, Comin R, Yuan M, Alarousu E, Buin A, et al. Low trap-state density and long carrier diffusion in organolead trihalide perovskite single crystals. Science 2015;347:519–22. doi:10.1126/science.aaa2725.
[16] Gevaerts VS, Koster LJA, Wienk MM, Janssen RAJ. Discriminating between Bilayer and Bulk Heterojunction Polymer:Fullerene Solar Cells Using the External Quantum Efficiency. ACS Appl Mater Interfaces 2011;3:3252–5. doi:10.1021/am200755m.
[17] Filipič M, Löper P, Niesen B, Wolf S De, Krč J, Ballif C, et al. CH3NH3PbI3 perovskite / silicon tandem solar cells: characterization based optical simulations. Opt Express 2015;23:A263--A278. doi:10.1364/OE.23.00A263.
[18] Johnson PB, Christy RW. Optical Constants of the Noble Metals. Phys Rev B 1972;6:4370–9. doi:10.1103/PhysRevB.6.4370.
[19] Hörantner MT, Leijtens T, Ziffer ME, Eperon GE, Christoforo MG, McGehee MD, et al. The Potential of Multijunction Perovskite Solar Cells. ACS Energy Lett 2017;2:2506–13. doi:10.1021/acsenergylett.7b00647.
[20] Löper P, Stuckelberger M, Niesen B, Werner J, Filipič M, Moon S-J, et al. Complex Refractive Index Spectra of $CH_3NH_3PbI_3$ Perovskite Thin Films Determined by Spectroscopic Ellipsometry and Spectrophotometry. J Phys Chem Lett 2015;6:66–71. doi:10.1021/jz502471h.
[21] Shin SS, Yeom EJ, Yang WS, Hur S, Kim MG, Im J, et al. Colloidally prepared La-doped BaSnO 3 electrodes for efficient , photostable perovskite solar cells 2017;6620.
[22] Prasanna R, Gold-Parker A, Leijtens T, Conings B, Babayigit A, Boyen HG, et al. Band Gap Tuning via Lattice Contraction and Octahedral Tilting in Perovskite Materials for Photovoltaics. J Am Chem Soc 2017;139:11117–24. doi:10.1021/jacs.7b04981.
[23] Shin SS, Yeom EJ, Yang WS, Hur S, Kim MG, Im J, et al. Colloidally prepared La-doped BaSnO3electrodes for efficient, photostable perovskite solar cells. Science 2017;356:167–71. doi:10.1126/science.aam6620.